Published in final edited form as:
AJR Am J Roentgenol. 2010 November ; 195(5): 1164–1174. doi:10.2214/AJR.09.3956.

Dual-source dual-energy CT with additional tin filtration: Dose and image quality evaluation in phantoms and in-vivo

Andrew N. Primak, PhD[1,2], **Juan Carlos Ramirez Giraldo**[1,3], **Christian D. Eusemann, PhD**[1,2], **Bernhard Schmidt, PhD**[4], **B. Kantor, MD**, **Joel G. Fletcher, MD**[1], and **Cynthia H. McCollough, PhD**[1,*]

[1] Department of Radiology, Mayo Clinic, Rochester, MN

[2] Siemens Medical Solutions USA, Malvern, PA

[3] Department of Physiology and Biomedical Engineering, Mayo Clinic, Rochester, MN

[4] Department of Cardiovascular Diseases, Mayo Clinic Rochester, MN

Abstract

Purpose—To investigate the effect on radiation dose and image quality of the use of additional spectral filtration for dual-energy CT (DECT) imaging using dual-source CT (DSCT).

Materials and Methods—A commercial DSCT scanner was modified by adding tin filtration to the high-kV tube, and radiation output and noise measured in water phantoms. Dose values for equivalent image noise were compared among DE-modes with and without tin filtration and single-energy (SE) mode. To evaluate DECT material discrimination, the material-specific DE_{ratio} for calcium and iodine were determined using images of anthropomorphic phantoms. Data were additionally acquired in 38 and 87 kg pigs, and noise for the linearly mixed and virtual non-contrast (VNC) images compared between DE-modes. Finally, abdominal DECT images from two patients of similar sizes undergoing clinically-indicated CT were compared.

Results—Adding tin filtration to the high-kV tube improved the DE contrast between iodine and calcium as much as 290%. Pig data showed that the tin filtration had no effect on noise in the DECT mixed images, but decreased noise by as much as 30% in the VNC images. Patient VNC-images acquired using 100/140 kV with added tin filtration had improved image quality compared to those generated with 80/140 kV without tin filtration.

Conclusion—Tin filtration of the high-kV tube of a DSCT scanner increases the ability of DECT to discriminate between calcium and iodine, without increasing dose relative to SECT. Furthermore, use of 100/140 kV tube potentials allows improved DECT imaging of large patients.

Keywords

Dual-energy CT; dual-source CT; material differentiation; beam filtration; CT image quality; CT radiation dose

Introduction

Although the theoretical basis for dual-energy CT (DECT) imaging was established in the late 1970's and early 1980's by Alvarez et al [1] and Kalender et al [2], it has been only since 2006

*Corresponding author: 200 First Street SW, Rochester, MN 55905, phone: 507-284-6875, fax: 507-284-2405, mccollough.cynthia@mayo.edu.

that DECT has made its way into routine clinical practice [3–17]. This "reincarnation" of DECT was facilitated by the commercial introduction of the first dual-source CT (DSCT) scanner in 2006 [18], which allowed simultaneous acquisition of high and low tube potential images. Alternative approaches for DECT imaging are under investigation, including rapid switching of the x-ray tube potential [2,19] and dual-layer (sandwich) detectors [20,21].

Both tubes of the first generation DSCT scanner (SOMATOM Definition, Siemens Healthcare, Forchheim, Germany) have the same beam filtration and generate identical x-ray spectra when operated at the same tube potential. Identical filtration is necessary for dual-source applications, where the data from both tubes can be combined to improve the temporal resolution of cardiac CT examinations. However, using the same filtration for both tubes provides less than optimal conditions for dual-energy (DE) acquisitions, where the two tubes are operated at different tube potentials. The x-ray spectra generated at low (80 kV) and high (140 kV) peak tube potentials have a high degree of spectral overlap, with a separation between the average energies of the two spectra of less than 30 keV (Figure 1).

It was first shown by Kelcz et al [22] that noise in the DE processed material-specific images, and hence the ability of DECT to discriminate between two materials, depends crucially on the difference between the DE_{ratio} of the materials. Here, DE_{ratio} represents a density-independent material-specific parameter. As shown in Figure 2, DE_{ratio} can be obtained experimentally by measuring the low and high-energy CT numbers (CT_{low} and CT_{high}) for several different densities of a given material, determining the slopes of the lines relating CT number to material density, and calculating the ratio of these slopes ($Slope_{low}/Slope_{high}$). The difference between the DE_{ratio} of two materials is determined by the separation between the high and low energy spectra and the effective atomic numbers of the evaluated materials. The smaller the spectral separation, the harder it is to discriminate between the materials, especially when they have close atomic numbers (e.g. calcium and iron).

Spectral separation can be increased by using additional filtration for one or both tube potentials. Previous research on optimizing the added filtration for DE imaging focused on dual-energy radiography applications, primarily chest radiography [23–25], mammography [26] and bone densitometry [27,28]. In contrast to dual-energy radiography, few studies have been published regarding optimization of the added filtration for DECT. In 1979, Kelcz et al [22] was the first to emphasize the importance of additional filtration for DECT performed using two unique tube potentials. Two additional studies examined the use of a split filter using a single source scanner [29], and a technique that changed beam filtration manually every 8 seconds [30].

For practical purposes, spectral separation of a DSCT system operated in the DE mode can be improved by hardening (i.e. increasing the mean energy of) the high-energy spectrum. Adding filtration to the low-kV tube is undesirable because it would further decrease the low-kV tube output, which is already insufficient (even at maximum tube current) for large patients. A recent simulation study [31] has shown that the use of added filtration for the high-kV tube can dramatically increase the DE contrast between clinically relevant materials (e.g., calcium and iodine) by decreasing spectral overlap (Figure 1). Although the simulations showed that seven single-element materials performed similarly well at proper thicknesses, tin was proposed as an ideal filter material, as it is inexpensive and easy to machine. Appropriate thicknesses were found to be 0.5 or 0.8 mm, respectively, for the large and normal size patient attenuations.

The purpose of this study was to experimentally validate these simulation results using a DSCT scanner that was modified to add tin filtration to the high-kV tube. We evaluated dose and image quality for images obtained on the same DSCT system, using both phantoms and live animals, and compared these results for images acquired in single energy (SE) mode and dual

energy (DE) modes both with and without the additional tin filtration. We further illustrate the potential of the method by comparing two patient abdominal DECT datasets, one with and one without tin filtration.

Materials and Methods

Tin filter

Factory assistance was obtained to install an additional tin filter on a commercial DSCT scanner (SOMATOM Definition DS, Siemens Healthcare, Forchheim, Germany). A flat tin filter of 0.4 mm thickness was attached to the bottom of the bow-tie filter located directly underneath the collimator of Tube A, which was operated at high-kV in the DE mode. The system was then recalibrated and tested for the accuracy of CT numbers. Although the simulation results [31] showed that the proper filter thickness depended on the amount of attenuation (e.g. 0.8 mm for normal body vs. 0.5 mm for large body), only one filter thickness (0.4 mm) was chosen for this study. Because having different thickness filters for different patient sizes adds considerable technical complexity, a single filter thickness of 0.4 mm was chosen for commercial implementation on the second generation DSCT system (SOMATOM Definition Flash, Siemens Healthcare, Forchheim, Germany). Although a thickness of 0.5 mm of tin was suggested by our simulations for relatively high attenuations (an anthropomorphic thorax phantom with a 40-cm lateral dimension), this thickness was reduced by 0.1 to 0.4 mm to provide increased tube output, which is required for DE imaging of patients larger than a 40-cm lateral dimension.

Phantom study

Scanner radiation output vs. noise—To compare radiation dose among the DE modes (80/140 kV and 100/140 kV) with and without tin filtration and the SE mode (120 kV), each at the same noise level, we measured noise and dose in each mode at different tube current-time product (mAs) values. Image noise was measured using cylindrical water phantoms of 3 different sizes: (Small) 20-cm diameter, (Medium) 30-cm diameter, and (Large) 30-cm diameter wrapped in a 4-cm thick layer of extra attenuating fat-mimicking material (Superflab, Radiation Product Design, Inc, Albertville, MN). Five different acquisition modes were used, as described in Table 1. The values for the ratio of Tube A effective mAs vs. Tube B effective mAs and the composition ratio were suggested by the manufacturer. Here, effective mAs equals mAs/pitch. The composition ratio (C_{ratio}) was used to produce linearly combined (mixed) images, according to equation:

$$\text{mixed image} = \text{Low} - \text{kV image} \times C_{ratio} + \text{High} - \text{kV image} \times (1 - C_{ratio}). \quad (1)$$

Specific composition ratios can be optimized, as shown by Yu et al [32]. The ratio of the effective mAs values for tubes A and B was selected to result in similar noise levels in the high- and low-kV images. All three water phantoms were scanned using the SE mode and the appropriately selected DE modes. Since the amount of power at 80 kV is sufficient to produce low noise images of the Small and Medium phantom, they were scanned at 80/140 kV with and without tin filtration. However, using 80 kV for the Large phantom would result in unacceptably high image noise, so it was scanned at 100/140 kV with and without tin filtration. The Medium phantom was additionally scanned at 100/140 kV with and without tin to allow comparison of the noise-matched dose values between the 80/140 kV and 100/140 kV acquisitions with and without the tin filter on a single phantom. For each of 11 phantom/acquisition mode combinations, five different scans were performed using low-kV tube effective mAs values of 100, 200, 300, 400 and 500 and 0.5 pitch. Contiguous images were

reconstructed using 3 mm slice thickness and a medium kernel (B40) for the Small and Medium phantoms, and 5 mm thickness and a medium smooth kernel (B30) for the Large phantom.

For the DE modes, only the combined (linearly mixed) images were used for the noise vs. dose evaluation. These images utilize the full dose of a DE scan resulting in a better image quality than either of the original (low and high kV) datasets and, hence, are used for routine diagnostic purposes as a substitute for conventional SE images [32,33]. A total of 55 image datasets (11 phantom/acquisition mode combinations × 5 scans) were analyzed. For each dataset, a 20-mm diameter circular region of interest (ROI) was placed in the center of the phantom and image noise was calculated as the standard deviation of the CT numbers within the ROI and averaged over 10 consecutive images.

The noise vs. dose study was designed to quantify how the addition of the tin filter affected noise for different size objects, provided that the scanner output remained unchanged. For this purpose, the volume CTDI ($CTDI_{vol}$), which is a measure of the scanner output, was used. $CTDI_{vol}$ corresponding to the five acquisition modes listed in Table 1 was measured in a 32-cm CTDI body phantom using the standard technique [34,35]. Image noise was then plotted against $CTDI_{vol}$ for all 11 phantom/acquisition mode combinations.

Effect of tin filter on DE material discrimination—To evaluate the effect of additional tin filtration on DE material discrimination, the DE_{ratio} values for calcium and iodine were measured using small and large (30 and 40 cm lateral dimension, respectively) anthropomorphic thorax phantoms (QRM, Möhrendorf, Germany) (Figure 3). The 10-cm cardiac insert of the phantom was replaced with a water-filled cylinder containing a custom Styrofoam frame. The frame was used to hold five 3-cc syringes filled with different known concentrations of iodine, and five cylinders with known calcium concentrations (courtesy of QRM). The syringes and the calcium cylinders were approximately 10 mm in diameter. The iodine solutions were prepared by diluting iodine contrast medium (Omnipaque 350, GE Healthcare) with water and had iodine concentrations from 3.5 to 17.5 mg/cm^3. The density of calcium in the QRM cylinders ranged from 50 to 900 mg/cm^3. The small thorax phantom was scanned using 80/140 kV with and without tin, while the large phantom was scanned using 100/140 kV with and without tin. One scan for each phantom/acquisition mode combination was performed using a low-kV tube effective mAs of 350 and a spiral pitch of 0.7; 5 mm axial images were reconstructed through the center of the calcium and iodine inserts for DE_{ratio} calculations. For every DE image set (high- and low-kV pair), the mean CT number in each calcium and iodine sample was measured and used to determine the slopes of the lines relating the CT numbers to material density, which were determined using linear regression and divided to obtain the DE_{ratio} (Figure 2).

Animal study

Institutional Animal Care and Use Committee approval was obtained for this study. Two female pigs (weight 38 and 87 kg) were studied. Both animals were tranquilized with intramuscular induction of telazol (5 mg/kg) and xylazine (2 mg/kg). They were then intubated and intravenous lines placed in their ears. The anesthesia was maintained during the entire study using intravenous ketamine (2 mg/kg), fentanyl (0.02 mg/kg), and etomidate (0.08 mg/kg) in normal saline (2–3 mL/min). Once prepared, the pig was placed in a supine position within the scanner. Electrodes on the limbs were used to monitor the heart rate. Animals were mechanically ventilated and their breathing was suspended during all scans using a large animal ventilator (model 613; Harvard Apparatus, Holliston, MA). After the study was completed, the anesthetized animal was euthanized with sodium pentobarbital (100 mg/kg).

The small animal was scanned using 80/140 kV with and without tin since the amount of power at 80 kV was sufficient to produce low noise 80 kV images. The large animal was scanned

using 100/140 kV with and without tin and 80/140 kV without tin. Our hypothesis was that without the tin filter, both the 80/140 kV and 100/140 kV acquisitions would produce suboptimal image quality compared to the 100/140 kV acquisitions with tin. One scan was acquired for each of the 5 animal/acquisition mode combinations using a low-kV tube effective mAs of 350, a spiral pitch of 0.7, and a 0.5 s rotation time. These settings correspond to the maximum power available for the low-kV tube. A higher power at low-kV could have been achieved by either decreasing the pitch or increasing the rotation time, but clinically, this would result in unacceptably long breathhold times for many body CT examinations. Automatic exposure control was not used, since it was not able to be programmed to account for the presence of the tin filter. The scanner radiation output ($CTDI_{vol}$) for each acquisition was recorded. The acquisition parameters are summarized in Table 2.

For all 5 scans, 80 mL or 90 mL of iodinated contrast material (Ultravist-300, Bayer HealthCare Pharmaceuticals Inc., Wayne, NJ) was injected into the ear vein using an injection rate of 3 or 5 mL/s for the small or large animal, respectively. Bolus tracking was used to trigger the scan when the iodine attenuation in the ascending aorta reached the pre-defined value of 100 HU (at 140 kV). Images were reconstructed using 3 mm slice thickness, 2 mm reconstruction interval and a medium smooth kernel that contained no edge enhancement (D30). Linearly mixed DE images were generated using the composition ratios listed in Table 2, and commercially-available 3-material decomposition software (Syngo DE, Siemens Healthcare, Forchheim, Germany) was used to produce iodine-subtracted “virtual non-contrast” (VNC) images. Therefore, for every animal scan (two for the small animal and three for the large animal), four image datasets (low-kV, high-kV, mixed, and VNC) were obtained, resulting in a total of 20 datasets.

Image noise for the mixed and VNC images was evaluated and compared between the 5 DE scans. Noise was measured by placing a circular ROI in a homogeneous region of the liver and recording the standard deviation of the CT numbers within the ROI. Images were also evaluated for the presence of artifacts and their severity.

Human study

IRB approval with waiver of informed consent was obtained for this HIPAA-compliant retrospective data analysis study. Patient A, 34 cm maximum lateral width, was scanned using a DSCT system (SOMATOM Definition DS, Siemens Healthcare, Forchheim, Germany) which has no added filtration. A DECT urogram was used to acquire 1) a DE non-contrast scan, and 2) a DE contrast-enhanced scan. Each scan used 80/140 kV without additional tin filtration (Table 3). Patient B, 36 cm maximum lateral width, was scanned using a newer-model DSCT system (SOMATOM Definition Flash, Siemens Healthcare, Forchheim, Germany) that had the capability to move 0.4 mm of tin into the high energy beam. A DECT urogram protocol was used to acquire 1) a SE non-contrast scan and 2) a DE contrast-enhanced scan. The DE scan used 100/140 kV with the tin filter (Table 3). Automatic exposure control (CareDose 4D, Siemens Healthcare, Forchheim Germany) was used for all scans. Images were reconstructed using a 1.5 mm slice thickness and a medium smooth, non-edge enhancing kernel (D30). Three-material decomposition was performed using the identical version of commercial software (Syngo DE VA31, Siemens Healthcare, Forchheim, Germany) to produce the iodine-subtracted VNC images. Axial and coronal VNC images were visually compared between the two patients.

The larger FOV of the second tube for the scans using the tin filter was not related directly to the presence of the tin filter, but rather was a consequence of the larger angular offset between the two tubes on the Definition Flash scanner compared to the Definition DS scanner. That is, the commercial product that incorporated the tin filter (Definition Flash) included other

technical modifications compared to the original dual source commercial product (Definition DS), one of which resulted in a larger field of view for the second tube.

Results

Noise in the water phantom as a function of $CTDI_{vol}$ is presented in Figure 4. These data were fit to a power curve, and the best fit equations used to calculate the dose values for a given noise level. Table 4 summarizes the $CTDI_{vol}$ values for the target noise levels corresponding to image noise obtained using the routine SE clinical abdominal protocol established in our practice (120 kV, 240 Quality reference mAs, 2×32×0.6 mm collimation, 0.5 s rotation time, CAREDose4D ON).

The results presented in Table 4 demonstrate that the SE mode provides the lowest noise-matched dose value only for the Small phantom. For the Medium and Large phantoms, at least one of the DE modes delivered less dose for the same noise compared to the SE mode. Between the two DE modes (with or without the tin filter), the tin filter reduced the dose for the Small phantom but increased it for the Large phantom. For the Medium phantom, the dose was larger with the tin filter for 80/140 kV acquisition mode but was similar with or without the tin filter using 100/140 kV.

The DE_{ratio} results obtained using the small and large thorax phantoms with iodine and calcium inserts are summarized in Table 5. With the additional tin filtration, the DE_{ratio} for the 80/140 kV mode (small phantom) increased from 1.64 to 2.01 for calcium and from 1.99 to 3.03 for iodine, while the DE_{ratio} for the 100/140 kV mode (large phantom) increased from 1.31 to 1.55 for calcium and from 1.55 to 2.20 for iodine. Therefore, adding the tin filter to the high-kV tube improved the DE_{ratio} difference between iodine and calcium from 0.35 to 1.02 (290%) for the 80/140 kV mode, and from 0.24 to 0.65 (270%) for the 100/140 kV mode.

The noise and $CTDI_{vol}$ results for the animal study are summarized in Table 6, and mixed and VNC images from the large animal are shown in Figure 5. The animal study showed that the mixed images with and without the tin filter have approximately the same noise at similar dose values. However, noise in the DE processed VNC images was about 30% lower when comparing 80/140 kV with and without tin, both at the same dose. VNC noise was about 20% lower for 100/140 kV with tin compared to 100/140 kV without tin, in spite of the fact the 100/140 kV with tin scan used about 20% lower dose (Table 6, Figure 5).

For the large animal, the images acquired at 80/140 kV without tin and 100/140 kV with tin used the maximum power available at low-kV. However, scans at 100/140 kV with the tin filter had approximately 70% higher radiation dose (25.0 vs. 14.6 mGy) and, hence, significantly less noise (13.2 vs 17.5HU) compared to the scans at 80/140 kV without the tin filter. The image artifacts observed in the original low-kV images for 80/140 kV scans without tin were due to insufficient x-ray power on the low-kV tube. These were essentially eliminated for the 100/140 kV scans with tin (Figure 6).

The VNC of patient B had improved image quality compared to that of patient A (Figure 7). Furthermore, VNC images of patient B better approximated the true non-contrast enhanced image compared to patient A (Figure 7). The difference in spectral separation did not directly affect the spatial resolution in the VNC images, even though the image without tin (Figure 7c) appears blurry relative to the image with tin (Figure 7a). Because the noise in DE material-specific images is increased compared to the original high- and low-kV images, some degree of smoothing is typically required during DE postprocessing, which can degrade spatial resolution. The VNC image from 100/140 kV with tin (Figure 7a) had lower noise and required less smoothing, resulting in improved spatial resolution compared to the VNC image from 80/140kV without tin (Figure 7c).

Discussion

The results of our study demonstrate that the addition of tin filtration to the high-energy x-ray tube provided a benefit for DE DSCT. It dramatically increased the difference between the DE_{ratio} for calcium and iodine, which is expected to enhance the performance of DE algorithms designed to discriminate between calcium (e.g. bone or calcified plaque) and iodinated contrast material. Also, DE DSCT with additional tin filtration delivered similar or less dose compared to conventional 120 kV SECT (Figure 4, Table 4). Therefore, the additional tin filter should facilitate improved clinical performance for DE applications, such as DECT angiography with automatic bone removal [36–39] and could be used routinely without incurring a dose penalty. Figure 8 uses a 3D volume display of a dual energy bone removal animal exam to demonstrate the improvement of overall image quality with use of the tin filter.

Although we experimentally measured only the DE_{ratio} for calcium and iodine, the increased separation between the high- and low-energy spectra provided by the tin filter will increase the difference between the DE_{ratio} for any two given materials. In our previous simulation work [31] we used slightly modified equations, first derived by Kelcz et al [22], to show that increasing the difference between the DE ratios simultaneously decreased noise in the DE material-specific images. In this study, we confirmed this result experimentally by comparing the noise level in the VNC (soft tissue-specific) images obtained with and without the tin filter at similar radiation dose. For the small pig, when scanned using 80/140 kV and the same dose level, the noise level of the VNC image using the tin filter was about 30% lower than without the tin filter. For the larger pig, when using 100/140 kV, the noise level in the VNC image was about 20% lower when using the tin filter, even though the dataset using the tin filter acquisition was acquired with approximately 20% less dose than the scan without the tin filter.

For the VNC of the large pig using 80/140 kV without tin, the noise was similar to that of 100/140 kV without tin, despite the fact the dose at 80/140 kV was about half that of at 100/140 kV. This is because the spectral separation was higher for the 80/140 kV case. Furthermore, the increased spectral separation at 100/140kV with tin provided a significantly lower noise VNC image.

As demonstrated by Eq. (6) in [31], the noise in any DE material-specific (e.g., VNC) images depends on two factors, the noise in the original high and low-energy images, which is determined by dose, and the DE contrast (difference between the DE ratios of the two materials), which is determined by the spectral separation and the effective atomic numbers of the two materials. For DE imaging, it is therefore essential to recognize that larger spectral separation increases the DE contrast, which is inversely proportional to the noise in the VNC image.

A significant advantage of the additional filtration is that it can substantially increase the number of patients which can be imaged with DECT. Currently, large patients are contraindicated for DECT because the 80/140 kV acquisition mode results in unacceptable noise in the 80 kV images, while the 100/140 kV mode does not provide sufficient DE contrast due to the small separation between the 100 and 140 kV spectra. Using a DSCT system with the additional tin filter minimizes this constraint. When operated at 100/140 kV with use of the tin filter, the system provided both sufficient power (photon flux) and DE contrast for imaging large patients. In fact, the difference between the DE_{ratio} of calcium and iodine was 86% higher (0.65 vs. 0.35) for the 100/140 kV mode with the tin filter compared to the 80/140 kV mode without the tin filter.

The benefit of using the tin filter for 100/140 kV scanning was illustrated in both the animal and patient studies. As shown in Figure 6, the image artifacts at 80 kV in the large pig due to insufficient tube power are eliminated at 100 kV. Although our patient data presents only an

illustration (only two patients are shown here), image quality for the VNC images at 100/140 kV with the tin filter was improved relative to the image quality achieved in a smaller patient at 80/140 kV without tin (Figure 7). Furthermore, large patients scanned at 100/140 kV with tin would receive significantly less dose for the same noise level compared to a conventional 120 kV SECT (Figure 4d, Table 4).

Based on our noise vs. dose results, the 100/140 kV plus tin scan mode is preferred for DE imaging using a DSCT system. The 80/140 kV mode provided significantly better DE contrast. However, for a medium size patient (attenuation equivalent to 30 cm of water), it resulted in a higher dose compared to 120 kV SECT at typical clinical settings (Figure 4b, Table 4). However, using the 100/140 kV with tin filter scan mode would deliver a smaller dose with respect to SECT (Figure 4c, Table 4). For the small patients (attenuation equivalent to 20 cm of water), the dose differences between the evaluated scan modes were small, with SE requiring the least dose, followed by 80/140 kV with tin.

Improved performance of DECT might allow development of new advanced clinical applications. For example, discriminating hemorrhagic iron from co-localized calcium inside individual plaques might be possible using DECT, provided that the specificity of the technique is sufficient to discriminate these two materials. This approach could be used for the non-invasive detection of vulnerable plaques, which are characterized by abnormal proliferation of vasa vasorum (micro-vessels running inside the vessel wall) and by intraplaque hemorrhage resulting in the accumulation of iron [40,41]. Another example is the improved characterization of renal stones. The current application available on a DSCT system can only reliably differentiate uric acid vs. non-uric acid stones [42,43]. The further discrimination of different types of non-uric acid stones (e.g., calcium-based stones vs. cystine vs. struvite) is compromised because these stones have similar DE_{ratio} values.

Only one particular thickness (0.4 mm) of the tin filter was used. Repeating the experiments using several different thickness values was prohibitively labor intensive. And, unless a system that allows multiple options for filter thickness (e.g. 0.4 vs 0.5 vs 0.8 mm) is commercialized, the thinnest filter must suffice for all patients in order to allow adequate tube output for large patients (i.e. 0.8 mm is too thick for use with large patients in the evaluated system with its current tube power specifications). The dose comparison and the dose vs. noise study were based on $CTDI_{vol}$, which is an approximation of the scan dose and has well known limitations [44]. Also, we did not investigate the effect of the tin filter on all possible types of DE material-specific post-processing algorithms (e.g. bone-removed, pseudo-monochromatic). However, our prior work [31] and that of Kelcz [22,31] indicate that increased spectral separation will improve any material-specific image processing tasks. Finally, the *in vivo* images obtained with and without the tin filter in the animal study did not necessarily have the same amount of iodine due to the presence of residual contrast material from prior injections in the later acquired scans, potential variations in animal physiology, and variations in scan delay times (determined by the bolus tracking software). For this reason, it was difficult to rigorously demonstrate the tin filter effect *in vivo*, although visual inspection of image quality provided convincing evidence in favor of the added tin filtration.

In conclusion, we have shown that the use of additional tin filtration in the high-energy beam of a DSCT system operated in the DE mode can dramatically increase the DE contrast between clinically relevant materials, with radiation dose being similar or lower than that from conventional SECT. The increase in the DE contrast should significantly improve the performance of DE material discrimination algorithms, increasing the clinical value of existing DE applications and opening possibilities for new advanced clinical applications. Furthermore, added filtration can be used with 100/140 kV tube potentials to allow improved DE imaging of large patients.

Acknowledgments

The project described was supported by Grant Number R01EB007986 from the National Institute of Biomedical Imaging and Bioengineering. The content is solely the responsibility of the authors and does not necessarily represent the official view of the National Institute of Biomedical Imaging and Bioengineering or the National Institutes of Health. This work was also supported by National Institute of Health grant RR-18898. The authors would like to thank Jill Anderson and Kay Parker for assistance with the animal preparation and Kristina Nunez for her help with manuscript preparation and submission.

References

1. Alvarez RE, Macovski AA. Energy-selective reconstructions in X-ray computerised tomography. Physics in Medicine and Biology 1976;21:733–744. [PubMed: 967922]
2. Kalender WA, Perman WH, Vetter JR, Klotz E. Evaluation of a prototype dual-energy computed tomographic apparatus. I. Phantom studies. Medical Physics 1986;13:334–339. [PubMed: 3724693]
3. Graser A, Johnson TR, Chandarana H, Macari M. Dual energy CT: preliminary observations and potential clinical applications in the abdomen. Eur Radiol 2009;19:13–23. [PubMed: 18677487]
4. Scheffel H, Stolzmann P, Frauenfelder T, et al. Dual-energy contrast-enhanced computed tomography for the detection of urinary stone disease. Invest Radiol 2007;42:823–829. [PubMed: 18007154]
5. Graser A, Johnson TR, Bader M, et al. Dual energy CT characterization of urinary calculi: initial in vitro and clinical experience. Invest Radiol 2008;43:112–119. [PubMed: 18197063]
6. Stolzmann P, Frauenfelder T, Pfammatter T, et al. Endoleaks after endovascular abdominal aortic aneurysm repair: detection with dual-energy dual-source CT. Radiology 2008;249:682–691. [PubMed: 18780822]
7. Chandarana H, Godoy MC, Vlahos I, et al. Abdominal aorta: evaluation with dual-source dual-energy multidetector CT after endovascular repair of aneurysms--initial observations. Radiology 2008;249:692–700. [PubMed: 18812561]
8. Boroto K, Remy-Jardin M, Flohr T, et al. Thoracic applications of dual-source CT technology. Eur J Radiol 2008;68:375–384. [PubMed: 18929452]
9. Pontana F, Faivre JB, Remy-Jardin M, et al. Lung perfusion with dual-energy multidetector-row CT (MDCT): feasibility for the evaluation of acute pulmonary embolism in 117 consecutive patients. Acad Radiol 2008;15:1494–1504. [PubMed: 19000866]
10. Fink C, Johnson TR, Michaely HJ, et al. Dual-Energy CT Angiography of the Lung in Patients with Suspected Pulmonary Embolism: Initial Results. Rofo. 2008
11. Thieme SF, Becker CR, Hacker M, Nikolaou K, Reiser MF, Johnson TR. Dual energy CT for the assessment of lung perfusion-Correlation to scintigraphy. Eur J Radiol 2008;68:369–374. [PubMed: 18775618]
12. Ruzsics B, Lee H, Zwerner PL, Gebregziabher M, Costello P, Schoepf UJ. Dual-energy CT of the heart for diagnosing coronary artery stenosis and myocardial ischemia-initial experience. Eur Radiol 2008;18:2414–2424. [PubMed: 18523782]
13. Schwarz F, Ruzsics B, Schoepf UJ, et al. Dual-energy CT of the heart-Principles and protocols. Eur J Radiol 2008;68:423–433. [PubMed: 19008064]
14. Chae EJ, Seo JB, Goo HW, et al. Xenon ventilation CT with a dual-energy technique of dual-source CT: initial experience. Radiology 2008;248:615–624. [PubMed: 18641254]
15. Chae EJ, Song JW, Seo JB, Krauss B, Jang YM, Song KS. Clinical utility of dual-energy CT in the evaluation of solitary pulmonary nodules: initial experience. Radiology 2008;249:671–681. [PubMed: 18796658]
16. Choi HK, Al-Arfaj A, Eftekhari A, et al. Dual Energy Computed Tomography in tophaceous gout. Ann Rheum Dis. 2008
17. Sun C, Miao F, Wang XM, et al. An initial qualitative study of dual-energy CT in the knee ligaments. Surg Radiol Anat. 2008
18. Flohr TG, McCollough CH, Bruder H, et al. First performance evaluation of a dual-source CT (DSCT) system. Eur Radiol 2006;16:256–268. [PubMed: 16341833]
19. Zou Y, Silver M. Analysis of fast kV-switching in dual energy CT using a pre-reconstruction decomposition technique. Proc SPIE 2008;6913:691313, 691311–691312.

20. Boll DT, Merkle EM, Paulson EK, Fleiter TR. Coronary stent patency: dual-energy multidetector CT assessment in a pilot study with anthropomorphic phantom. Radiology 2008;247:687–695. [PubMed: 18424688]
21. Boll DT, Merkle EM, Paulson EK, Mirza RA, Fleiter TR. Calcified vascular plaque specimens: assessment with cardiac dual-energy multidetector CT in anthropomorphically moving heart phantom. Radiology 2008;249:119–126. [PubMed: 18710959]
22. Kelcz F, Joseph PM, Hilal SK. Noise considerations in dual energy CT scanning. Med Phys 1979;6:418–425. [PubMed: 492076]
23. Gauntt DM, Barnes GT. X-ray tube potential, filtration, and detector considerations in dual-energy chest radiography. Medical Physics 1994;21:203–218. [PubMed: 8177153]
24. Ducote JL, Xu T, Molloi S. Optimization of a flat-panel based real time dual-energy system for cardiac imaging. Medical Physics 2006;33:1562–1568. [PubMed: 16872063]
25. Shkumat NA, Siewerdsen JH, Dhanantwari AC, et al. Optimization of image acquisition techniques for dual-energy imaging of the chest. Medical Physics 2007;34:3904–3915. [PubMed: 17985636]
26. Boone JM, Shaber GS, Tecotzky M. Dual-energy mammography: A detector analysis. Medical Physics 1990;17:665–675. [PubMed: 2215412]
27. Skipper, JA.; Hangartner, TN. Optimizing X-ray spectra for dual-energy radiographic bone densitometry. Proceedings of the 15th Southern Biomedical Engineering Conference; Piscataway, NJ: IEEE; 1996. p. 297-300.
28. Herve L, Robert-Coutant C, Dinten J-M, Verger L, Comparat V. Optimization of x-ray spectra for bone mineral density and body composition measurements: theoretical study and experimental validation. Proc SPIE Int Soc Opt Eng 2002;4786:132–143.
29. Rutt B, Fenster A. Split-Filter Computed Tomography: A Simple Technique for Dual Energy Scanning. Journal of Computer Assisted Tomography 1980;4:501–509. [PubMed: 7391293]
30. Marshall W, Hall E, Doost-Hoseini A, Alvarez R, Macovski A, Cassel D. An implementation of Dual Energy CT Scanning. Journal of Computer Assisted Tomography 1984;8:745–749. [PubMed: 6736377]
31. Primak AN, Ramirez Giraldo JC, Liu X, Yu L, McCollough CH. Improved dual-energy material discrimination for dual-source CT by means of additional spectral filtration. Med Phys 2009;36:1359–1369. [PubMed: 19472643]
32. Yu L, Primak A, Liu X, McCollough C. Image quality optimization and evaluation of linearly-mixed images in dual-source, dual-energy CT. Med Phys 2009;36:1019–1024. [PubMed: 19378762]
33. Behrendt FF, Schmidt B, Plumhans C, et al. Image fusion in dual energy computed tomography: effect on contrast enhancement, signal-to-noise ratio and image quality in computed tomography angiography. Invest Radiol 2009;44:1–6. [PubMed: 19060790]
34. American Association of Physicists in Medicine. The measurement, reporting and management of radiation dose in CT. AAPM Task Group 23 of the Diagnostic Imaging Council CT Committee; College Park, MD. 2008.
35. International Electrotechnical Commission. IEC publication No. 60601–2-44. 2.1. International Electrotechnical Commission (IEC) Central Office; Geneva, Switzerland: 2002. Medical Electrical Equipment. Part 2–44: Particular requirements for the safety of x-ray equipment for computed tomography.
36. Meyer BC, Werncke T, Hopfenmuller W, Raatschen HJ, Wolf KJ, Albrecht T. Dual energy CT of peripheral arteries: Effect of automatic bone and plaque removal on image quality and grading of stenoses. Eur J Radiol 2008;68:414–422. [PubMed: 18963674]
37. Tran DN, Straka M, Roos JE, Napel S, Fleischmann D. Dual-energy CT discrimination of iodine and calcium: experimental results and implications for lower extremity CT angiography. Acad Radiol 2009;16:160–171. [PubMed: 19124101]
38. Watanabe Y, Uotani K, Nakazawa T, et al. Dual-energy direct bone removal CT angiography for evaluation of intracranial aneurysm or stenosis: comparison with conventional digital subtraction angiography. Eur Radiol. 2008
39. Brockmann C, Jochum S, Sadick M, et al. Dual-Energy CT Angiography in Peripheral Arterial Occlusive Disease. Cardiovasc Intervent Radiol. 2009

40. Kolodgie FD, Gold HK, Burke AP, et al. Intraplaque hemorrhage and progression of coronary atheroma. N Engl J Med 2003;349:2316–2325. [PubMed: 14668457]

41. Langheinrich AC, Michniewicz A, Sedding DG, et al. Quantitative X-ray imaging of intraplaque hemorrhage in aortas of apoE(−/−)/LDL(−/−) double knockout mice. Invest Radiol 2007;42:263–273. [PubMed: 17414521]

42. Primak AN, Fletcher JG, Vrtiska TJ, et al. Noninvasive differentiation of uric acid versus non-uric acid kidney stones using dual-energy CT. Acad Radiol 2007;14:1441–1447. [PubMed: 18035274]

43. Stolzmann P, Scheffel H, Rentsch K, et al. Dual-energy computed tomography for the differentiation of uric acid stones: ex vivo performance evaluation. Urol Res 2008;36:133–138. [PubMed: 18545993]

44. American Association of Physicists in Medicine. The measurement, reporting and management of radiation dose in CT (Report #96). AAPM Task Group 23 of the Diagnostic Imaging Council CT Committee; College Park, MD. 2008.

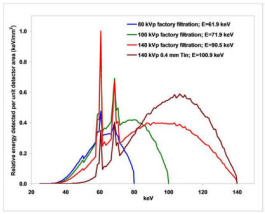

Figure 1.

Simulated x-ray spectra for a DSCT system at 80, 100 and 140 kV with the factory supplied filtration and at 140 kV with the addition of 0.4 mm of tin filtration. Details of this simulation are described elsewhere [31]. The mAs ratios used for the simulation correspond to clinical DE abdominal protocols in our practice. The mean energy E was calculated according to Eq. (8) in [31]. [Note: authors agree to pay for color reproduction].

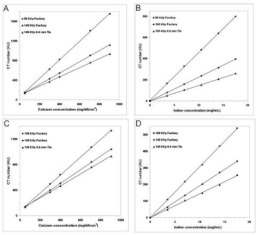

Figure 2.
Plots of CT number vs. material concentration for (a, c) calcium and (b, d) iodine obtained using (a, b) 80/140 kV with 30-cm phantom and (c, d) 100/140 kV with 40-cm phantom with and without the tin filter. Linear regressions were used to determine the slopes. The ratio of the slopes ($slope_{low}/slope_{high}$) is referred to as the DE_{ratio}.

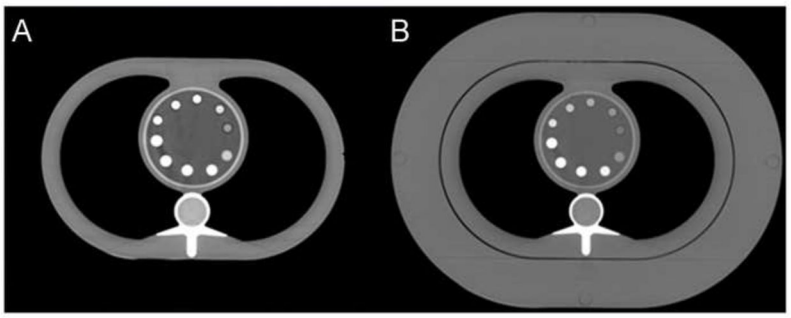

Figure 3.
Axial images of the (a) small and (b) large anthropomorphic thorax phantom used for DE_{ratio} measurements. The small phantom had a lateral dimension of 30 cm and was used for the 80/140 kV acquisitions. The large phantom had an additional attenuating layer, extending its lateral size to 40 cm; this phantom was used for the 100/140 kV acquisitions. The central water-filled portion of the phantom contained 10 inserts with different known concentrations of calcium and iodine.

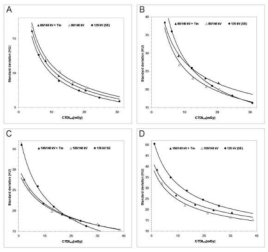

Figure 4.
The noise vs. dose curves obtained using Small, Medium and Large water phantoms: (a) the Small phantom data for scans using 120 kV and 80/140 kV with and without tin; (b) the Medium phantom data for scans using 120 kV and 80/140 kV with and without tin; (c) the Medium phantom data for scans using 120 kV and 100/140 kV with and without tin; and (d) the Large phantom data for scans using 120 kV and 100/140 kV with and without tin. The solid lines represent a fit of the data to a power-law curve.

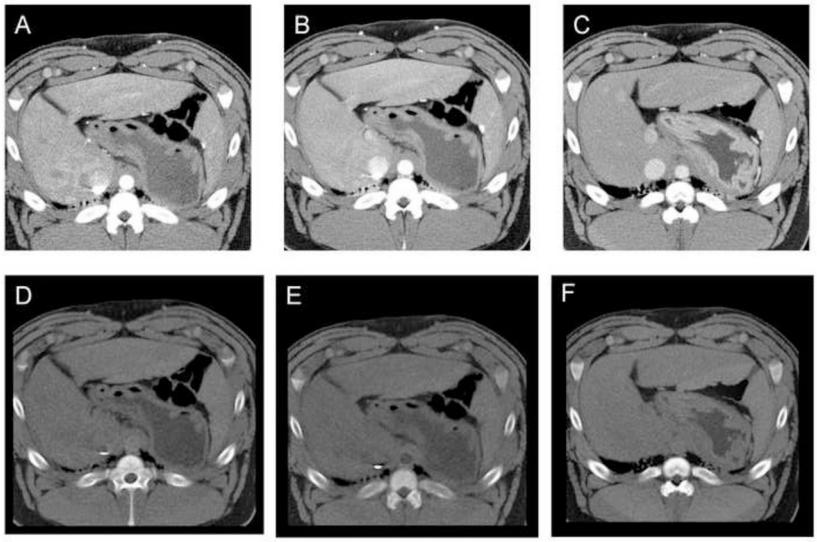

Figure 5.
Mixed (a–c) and virtual (d–f) non-contrast enhanced images before and after the addition of 0.4 mm of tin in an 87 kg pig. (a,d) 80/140 kV; (b,e) 100/140 kV; and (c,f) 100/140 kV plus tin. Notice similar image quality for a–c (mixed images) but significantly better image quality for (f) VNC images using the tin filter.

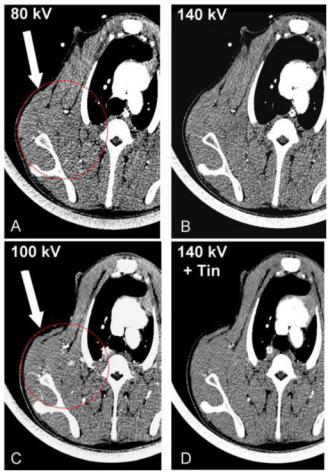

Figure 6.
The original (low- and high-kV) images of the large animal acquired using (a, b) 80/140 kV without the tin filter and (c, d) 100/140 kV with the tin filter, both using maximum power for the low kV tubes. The DE scan acquired (a) using 100/140 kV with tin had approximately double the total amount of radiation dose and, hence, (c) the corresponding low-kV images had significantly less noise compared to (a) the low-kV images acquired using 80/140 kV without tin. The image artifacts observed in (a) due to insufficient x-ray power were essentially eliminated in (c) (see arrows).

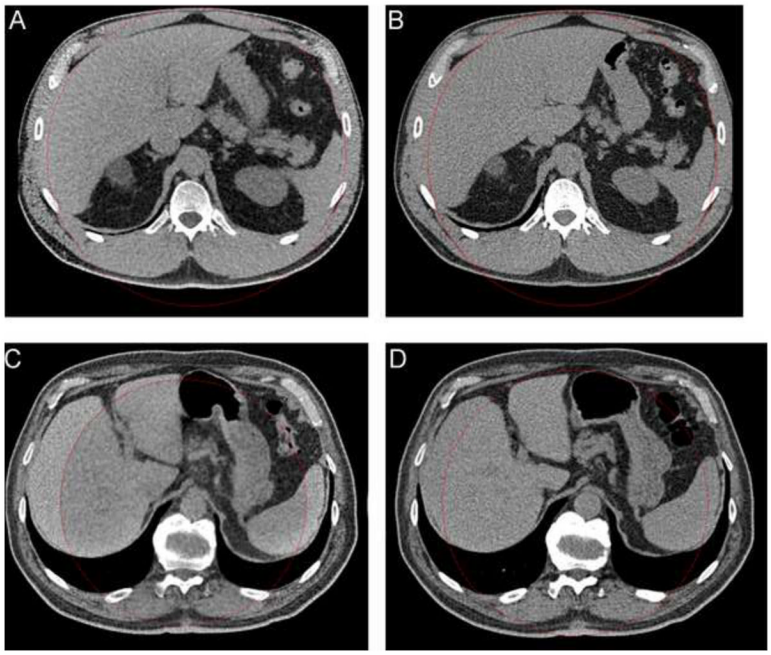

Figure 7.
Virtual non-contrast (VNC) images obtained using (a) 100/140 kV with tin correlated well with (b) the true non-contrast enhanced scan. (c) The VNC image obtained using 80/140 kV without tin was notably inferior in spatial resolution and CT number homogeneity compared to (d) the true non-contrast scan, even though the relatively thin patient (34 cm lateral width) was smaller than the patient shown in (a, b) (36 cm lateral width). The dotted circle represents the field of view of the second tube/detector pair, which was larger on (a) the scanner equipped with the tin filter (33 cm) than in (c) the scanner without the tin filter (26 cm).

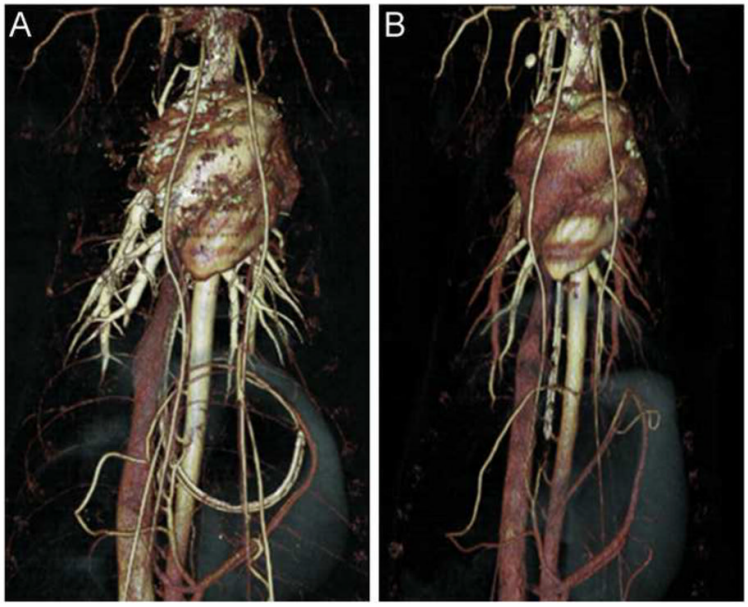

Figure 8.
3D volume-rendered images from the 38 kg pig obtained (a) 80/140 kV without tin and (b) 100/140 kV with tin. Bone removal was automatically performed by exploiting the difference in the DE ratio between calcium and iodine.

AJR Am J Roentgenol. Author manuscript; available in PMC 2010 November 1.

Table 1

The acquisition parameters for the five acquisition modes used in the phantom study. The values for the ratio of Tube A effective mAs vs. Tube B effective mAs, and the composition ratio were suggested by the manufacturer.

Acquisition parameters	**Acquisition Mode**				
	SE	**80/140 kV**	**100/140 kV**	**80/140 kV+Tin**	**100/140 kV + Tin**
Phantom size (S, M, L)	**S, M, L**	**S and M**	**M and L**	**S and M**	**M and L**
Tube A potential (kV)	120	140	140	140	140
Tube B potential (kV)	-	80	100	80	100
Tin filter (Y or N)	N	N	N	Y	Y
Ratio of Tube A eff mAs vs. Tube B eff mAs*	-	0.24	0.5	0.7	1.0
Collimation (mm)	24×1.2	14×1.2	14×1.2	14×1.2	14×1.2
Rotation time (s)	0.5	0.5	0.5	0.5	0.5
Composition ratio**	-	0.3	0.3	0.4	0.6
Automatic exposure control (Y or N)	N	N	N	N	N

*eff mAs=effective mAs=mAs/pitch

**Composition ratio was used to produce the linearly-mixed images according to Eq. (1).

- indicates not applicable.

Table 2

Acquisition parameters for the animal study

Acquisition parameters	Acquisition Mode			
	80/140 kV	100/140 kV	80/140 kV + Tin	100/140 kV + Tin
Animal size (S, L)	**S and L**	**L**	**S**	**L**
Tube A potential (kV)	140	140	140	140
Tube B potential (kV)	80	100	80	100
Tin filter (Y or N)	N	N	Y	Y
Tube A eff mAs/Tube B eff mAs*	84/350	175/350	245/350	350/350
Collimation (mm)	14×1.2	14×1.2	14×1.2	14×1.2
Rotation time (s)	0.5	0.5	0.5	0.5
Pitch	0.7	0.7	0.7	0.7
Composition ratio**	0.3	0.3	0.4	0.6
DE_{ratio} for VNC processing	2.0	1.6	3.0	2.2
Automatic exposure control (Y or N)	N	N	N	N
$CTDI_{vol}$ (mGy)	14.6	30.6	14.3	25.0

* eff mAs=effective mAs=mAs/pitch

** Composition ratio was used to produce the linearly-mixed images according to Eq. (1).

Table 3

Acquisition parameters for the human study

Acquisition Parameters	Non Contrast Exam		Contrast Enhanced Exam	
	Patient A	Patient B	Patient A	Patient B
Protocol	Dual Energy	Single Energy	Dual Energy	Dual Energy
Tube potential (kV)	80/140	120	80/140	100/140
Tin filter (Y or N)	N	N	N	Y
DE_{ratio} for VNC processing	-	-	2.0	2.2
Collimation (mm)	14 × 1.2	128 × 0.6	14×1.2	32×0.6
Tube A eff mAs/Tube B eff mAs*	82/372	343/-	82/372	218/170
Pitch	0.7	0.55	0.7	0.6
Rotation time (s)	0.5	0.5	0.5	0.5
Composition ratio**	0.5	-	0.5	0.5
Maximum DE Field of View (cm)	26	-	26	33
Automatic exposure control (Y or N)	Y	Y	Y	Y
$CTDI_{vol}$ (mGy)	15.2	14.0	13.1	16.9

* eff mAs=effective mAs=mAs/pitch

** Composition ratio was used to produce the linearly-mixed images according to Eq. (1).

- indicates data not acquired or not applicable.

Table 4

The scanner radiation output ($CTDI_{vol}$ in mGy) required to achieve the target noise levels for the small, medium and large water phantoms. The target noise levels corresponded to the image noise obtained using our practice's routine single-energy clinical abdominal protocol. Lowest $CTDI_{vol}$ values are bolded. For the Medium and Large phantom, 100/140 kV required the lowest dose. However, the DE contrast between iodine and calcium is low at this setting. With the addition of the tin filter, the DE contrast is strongly improved, and DE material decomposition is possible, even though the total $CTDI_{vol}$ is lower than for SECT.

Water phantom	Target noise level (HU)	120 kV	80/140 kV	100/140 kV	80/140 kV + Tin	100/140 kV + Tin
Small	14.4	**4.6**	5.8	-	5.2	-
Medium	21.0	18.4	16.7	**15.4**	21.8	16.4
Large	22.8	28.2	-	**17.3**	-	21.3

- indicates data not acquired.

Table 5

DE ratios and the difference between them for calcium and iodine obtained using the factory-installed filtration, which was identical on both tubes, and an additional 0.4 mm of tin filtration on the high kV tube.

	Small thorax phantom		Large thorax phantom	
Scan mode	80/140 kV	80/140 kV + Tin	100/140 kV	100/140 kV + Tin
Ca	1.64	2.01	1.31	1.55
I	1.99	3.03	1.55	2.20
Difference	0.35	1.02	0.24	0.65

Table 6

$CTDI_{vol}$ (mGy) and noise (Standard Deviation of CT numbers, HU) the animal scans. Using the same $CTDI_{vol}$ for the small animal, the noise in the mixed images was equivalent with or without tin, while noise in the VNC image was reduced with tin. For the large animal, tube power limitations prevented obtaining sufficient tube output at 80/140 kV, hence the $CTDI_{vol}$ value was unchanged from the small animal, and the noise was almost doubled. At 100/140 kV, however, even though using less dose with the tin filter, the noise in the mixed images was the same with and without tin, and the noise in the VNC images was decreased with tin.

Animal size	Image type	80/140 kV		100/140 kV		80/140 kV + Tin		100/140 kV + Tin	
		$CTDI_{vol}$	Noise	$CTDI_{vol}$	Noise	$CTDI_{vol}$	Noise	$CTDI_{vol}$	Noise
Small	Mixed	14.6	9.2	-	-	14.3	9.0	-	-
Small	VNC		9.9		-		7.1		-
Large	Mixed	14.6	17.5	30.6	13.0	-	-	25.0	13.2
Large	VNC		17.6		18.4		-		14.5

- indicates data not acquired.